A stability and spatial-resolution enhanced laser absorption spectroscopy tomographic sensor for complex combustion flame diagnosis

Rong Zhao [a], Bin Zhou [a,*], Jianyong Zhang [b], Ruixue Cheng [b], Qi Liu [a], Minglu Dai [a], Bubin Wang [a], Yihong Wang [a]

[a] *School of Energy and Environment, Southeast University, Nanjing, 210096, China*
[b] *School of Computing, Engineering and Digital Technologies, Teesside University, Middlesbrough, TS1 3BX, UK*

A B S T R A C T

A novel stable laser absorption spectroscopy (LAS) tomographic sensor with enhanced stability and spatial resolution is developed and applied to complex combustion flame diagnosis. The sensor reduces the need for laser collimation and alignment even in extremely harsh environments and improves the stability of the received laser signal. Furthermore, a new miniaturized laser emission module was designed to achieve multi-degree of freedom adjustment. The full optical paths can be sampled by 8 receivers, with such arrangement, the equipment cost can be greatly reduced, at the same time, the spatial resolution is improved. In fact, 100 emitted laser paths are realized in a limited space of 200mm×200 mm with the highest spatial resolution of 1.67mm×1.67 mm. The stability and penetrating spatial resolution of the LAS tomographic sensor were validated by both simulation and field experiments on the afterburner flames. Tests under two representative experiment states, i.e., the main combustion and the afterburner operation states, were conducted. Results show that the error under the main combustion state was about 4.32% and, 5.38% at the afterburner operation state. It has been proven that this proposed sensor can provide better tomographic measurements for combustion diagnosis, as an effective tool for improving performances of afterburners.

1. Introduction

Combustion is a complex phenomenon with multi-physical coupled fields. The process and products of combustion can directly characterize the state of the combustion flow field, including combustion stability, combustion efficiency, flame structure [1–4]. Many non-invasive techniques have been adopted to study the flame characteristics, such as the acoustic method [5–8], coherent anti-stokes raman scattering spectrometry (CARS) [9], planar laser induced fluorescence (PLIF) [3], and tunable diode laser absorption spectroscopy (TDLAS) [10,11].

Compared to other non-contact combustion diagnostic techniques, LAS technology has the advantages of non-invasive measurement, high selectivity, high measurement accuracy, multi-parameter detection, environmental adaptability, and suitability for industrial applications. Due to the non-uniform characteristics of the fluid field, in order to accurately obtain the spatial distribution of its temperature and concentration, the LAS technique is combined with computed tomography (CT) technique to measure the two-

---

dimensional distribution, which is known as laser absorption tomography (LAT) [12–15].

Due to the harsh combustion environments, any aero-engine combustion chamber has problems such as severe mechanical vibrations and turbulent combustion, which can severely affect the stability of the laser signal in an embedded TDLAS diagnosis sensor. The limited space constrains the maximum number of optical sensors to be installed in design. To optimize performance or minimize sensors in combustion systems, some designers are alternatively direct their efforts toward optimizing sensor distribution for a given limited number of sensors. In LAS tomographic sensor, a parallel, or a fan-shaped, or an irregular and sparse beam arrangement is usually adopted. However, the parallel laser beam arrangement has usually fewer light paths, so it suffers from serious ill-posed problem. For the fan beam arrangement, although the cost of installing emitters can be reduced, it often has the corner distortion in the reconstructed image. The beam splitters [16–19] used in the parallel arrangement or the cylindrical lens [20–22] in the fan arrangement can significantly reduce laser power, leading to a lower signal-to-noise ratio in the reconstruction. The irregular laser beam arrangement was also employed [23,24] with an optimization strategy to reduce the number of beams and determine the optimal beam position. However, such an arrangement usually requires a complex optical system. The ability of tomography system to resolve increasingly smaller features within the region of interest determines its suitability for studying reactive flows. The increase in spatial resolution is achieved either by intensive sampling of the region of interest or by data analysis and image processing. Regardless of the data analysis and image reconstruction algorithm, there is a motivation to maximize the number of experimental measurements, as this allows the subsequent algorithmic analysis to be optimal. Among the reported TDLAS tomographic measurements, Zhao et al. [25] discretized into 900 grids by an-shaped laser beams in a circle with a diameter of 150 mm. Shui et al. [26] discretized the reconstructed domain into 40×40 grids in the numerical simulation, and the region of interest was set as an 80 mm×80 mm square and divided into 20×20 grids. Song et al. [27] divided into 31×31 grids in the rectangular region of interest.

From the above review of existing beam arrangements, it is apparent that a LAS tomography system with a simpler structure, enhanced stability and good spatial resolution for afterburner flame measurement is desirable. The system proposed in this paper can fulfil such attributes. The receiver of the sensor is formed using an integrating sphere of a 12 mm diameter receiving surface plus a detector, and a uniformly distributed laser beam is created through multiple reflections from the inner wall of the sphere. The advantage of this novel arrangement is that the requirement for laser collimation and alignment is much less critical even in extremely harsh environments, so that interference fringes are avoided and the stability of the laser signal is improved. Furthermore, in this system, a new purposely designed miniaturized laser emission module is implemented to enable multi-degree of freedom adjustment so as to yield a reduced signal power attenuation. The full optical paths of a typical afterburner flame can be sampled using only 8 sets of receivers, and the spatial resolution has been significantly improved compared with other LAS tomography beam arrangements by scanning. In fact, 100 emitted laser paths have been realized in a limited space of 200mm×200 mm with a spatial resolution of 1.67mm×1.67 mm. A prototype of this sensor has been developed and validated through both simulation and full-scale field tests. The designed sensor is capable of providing parameters for diagnosing combustion effectively and accurately, forming important information for improving performances of afterburner. At present, the sensor is adapted for quasi-steady-state measurement, however a higher-speed laser switcher can be used to boost the image reconstruction for dynamic applications.

2. Theoretical principle

This section provides a brief summary of the theories of 2D temperature measurements based on the laser absorption spectroscopy and computed tomography.

According to the Beer-Lambert law, the spectroscopic absorbance $a(v)$ at wave number ν can be expressed as:

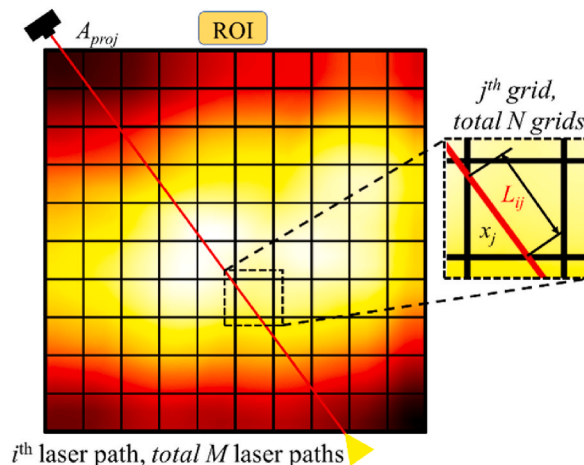$$\alpha(v) = -\ln\left(\frac{I_t(v)}{I_0(v)}\right) = \int_0^L P(l)X(l)S_v(T(l))\varphi(v,l)dl \tag{1}$$

Fig. 1. Schematic diagram of discrete configuration and single laser beam projection.

where $I_0(v)$ and $I_t(v)$ are the incident and transmitted laser intensities at v, respectively, $P(l)$ [atm] is the local total pressure, and l is the position along the path. $X(l)$ represents the local molar fraction of the absorbing species, $T(l)$ [K] is the local temperature, $\varphi(v, l)$ [cm] denotes the line shape function, and $S(T)$ [cm^{-2}atm^{-1}] stands for the temperature-dependent line strength. The line shape φ is no longer a standard Voigt function, but its integral over wave number is equal to 1. Hence the integral absorbance over the entire wave number range, A can be derived from Eq. (1) as :

$$A = \int_0^L P(l)X(l)S_v(T(l))dl \tag{2}$$

For the complex combustion field, as shown in Fig. 1, the region of interest (ROI) is discretized into N grids and crossed by M laser paths in total for tomographic reconstruction. In each grid, the flame parameters such as pressure, temperature, and gas concentration are assumed to be constant. On the ith laser path, the integral absorbance with the wave number v, $A_{v,i}$ can be expressed as :

$$A_{v,i} = \sum_{j=1}^{N} PS(T_j)X_j l_{ij} = \sum_{j=1}^{N} \alpha_{v,j} l_{ij} \tag{3}$$

where $\alpha_{v,j}$ is the local integral absorbance in the jth grid at the wavenumber v, j represents the grid number ($j = 1, 2, \ldots N$), and l_{ij} is the length of the ith laser path crossing the jth grid. For LAS tomography, Eq. (3) can be rewritten as the following matrix form for efficient computation,

$$\boldsymbol{L\alpha_v = A_v} \tag{4}$$

where $\boldsymbol{L}$ stands for the sensitivity matrix with dimension of $M \times N$, M the number of laser paths, N the number of grids, which is calculated prior to the measurements based on the geometric distribution of the lasers, and both $\boldsymbol{\alpha} = \{\alpha_{v,1}, \alpha_{v,2}, \alpha_{v,N}\}^T$, the spectroscopic absorbance, and $\boldsymbol{A} = \{A_{v,1}, A_{v,2}, A_{v,N}\}^T$, the integrated absorbance in Eq. (4) are column vectors. When $\boldsymbol{\alpha_v}$ of the target species at two or more wave numbers are obtained through measurements, from which the distributions of the flame parameters of temperature and gas concentration can be extracted. The temperature at the jth grid can be calculated from the ratio of the reconstructed $\alpha_{v1,j}$, $\alpha_{v2,j}$ at two preselected transitions wave numbers (v_1 and v_2) with the two different temperature dependencies as follows,

$$T_j = \frac{hc}{k}\left(E_{2,j}'' - E_{1,j}''\right)\left[\ln\frac{\alpha_{v1,j}}{\alpha_{v2,j}} + \ln\frac{S_{2,j}(T_0)}{S_{1,j}(T_0)} + \frac{hc}{k}\left(\frac{E_{2,j}'' - E_{1,j}''}{T_0}\right)\right]^{-1} \tag{5}$$

When the gas temperature is found, species concentration X_j can then be determined by using Eq. (6)

$$X_j = \frac{\alpha_j}{P_j l_j S(T_j)} \tag{6}$$

The local integral absorbance α can be reconstructed by implementing the specific tomographic algorithms. Here, the modified algebraic reconstruction technique (ART) is utilized to obtain smooth reconstruction of images, details of the method can be found in Refs. [27,28]. The focus of this paper is on the introduction of diagnosis sensor, rather than the details of the reconstruction algorithm. The iteration is formulated as follows,

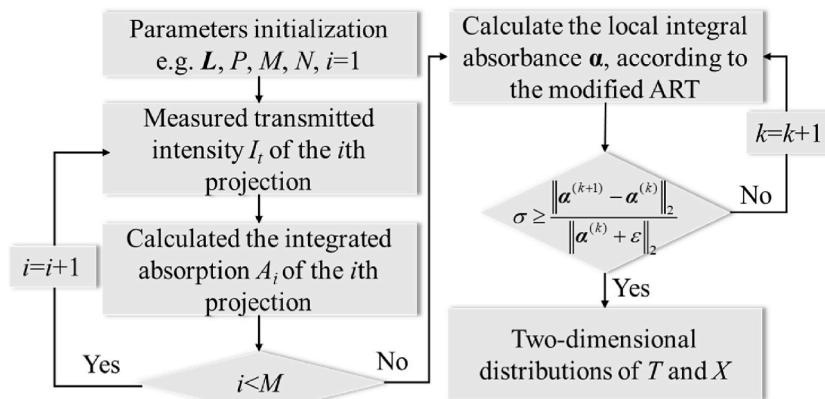$$\alpha^{(k+1,i)} = \alpha^{(k,i)} - \lambda\left(L_i \alpha^{(k,i)} - A_i\right) \tag{7}$$

where

Fig. 2. Flow chart of temperature and gas concentration distributions reconstructions.

$$\lambda = \beta \times \frac{\alpha_j^{(k)} L_{ij}}{\sum\limits_{j=1}^{N} \alpha_j^{(k)} L_{ij}} \tag{8}$$

k in Eq. (8) indicates the current iteration step, A_i is the ith element of the absorbance; and λ is the relaxation factor, and $\lambda \in (0, 2)$, which is used to control the convergence rate. This algorithm is used to correct the relaxation factor λ. β in Eq. (7) is generally obtained empirically, and in this paper it is determined through least squares optimization, and the optimal value is 0.01. The flow chart of the temperature and gas concentration distribution reconstruction is shown in Fig. 2.

3. Sensor design

3.1. Selection of absorption lines

H$_2$O vapor is a major product of the combustion of hydrocarbons. Its absorption spectrum is strong at near-infrared wavelengths. Therefore, H$_2$O vapor was chosen as the target absorbing species. The selection of an optimal H$_2$O spectral line pair is important in the design of absorption two-line thermometry, which were discussed in details elsewhere [15]. In this work, the line pair of 7185.60 cm^{-1} and 7444.36 cm^{-1} was selected to infer temperature by means of two-line scheme. According to the HITRAN database [29], there should be several neighbor transitions, with parameters detailed in Table 1, interfering the target transitions. For each transition, the table shows its wavenumbers, line strengths ($S(T_0)$) at $T_0 = 296$ K, pressure broadening-induced half-widths for itself (ξ_{self}) and air (ξ_{air}), energies of the lower-state (E''), and coefficients of temperature dependent broadening (n_{air}). In Table 1, the absorption lines 7185.596 cm^{-1} and 7185.597 cm^{-1} belong to the same vibrational band, but the absorptions are slightly staggered by the reversal of the up and down dynamics of the leap, because they are very close to each other and have the same low-state energy level and pressure spreading coefficient, so they are treated directly as a single absorption without other effects, and are considered to as one line. Similarly, the absorption lines 7444.351 cm^{-1}, 7444.368 cm^{-1} and 7444.371 cm^{-1} are considered as one line.

Fig. 3 shows the two relevant H$_2$O absorption lines at different temperatures and a particular concentration. The absorbance of the absorption lines near the two transitions is close to one order of magnitude smaller at different temperatures. And these two transitions are also relatively-well isolated from nearby absorption lines so that the data reduction becomes easier. Fig. 4 shows the line strengths and ratio of the line strengths of these two H$_2$O absorption transitions at 7185.60 cm^{-1} and 7444.36 cm^{-1}. The plotted temperature range varied from 296 K to 2500 K in consideration of practical combustion environments. As we can see from Fig. 4, the line pair we selected has sufficient absorption line strength and temperature sensitivity.

3.2. Evaluation of the effectiveness and robustness of the designed sensor

In order to assess the effectiveness and robustness of the designed sensor, mathematical models of temperature and molar concentration of water vapor for two representative combustion states were established for the flame combustion characteristics of the afterburner. As shown in Fig. 7(a) and (d), at the first state, the flame distribution was simulated with the main combustion chamber in operation only was assumed, the combustion flame field distribution was fitted with a hyperboloid distribution. The three-dimensional Gaussian distribution was used to simulate the combustion flame field distribution at the second state. The two distributions were superimposed together to constitute the flame reaction stream distribution. According to some classical combustion field parameters of the afterburner, the temperature and the concentration ranges should be 600–1200 K and, 0.02–0.05 mol/mol, respectively. The specific fields were obtained by using Eqs. (9) and (10). The exact temperature and water vapor concentration distributions are depicted in Fig. 6(a) and (d).

$$T = 600 + 1200 \cdot F \tag{9}$$

$$C = 0.02 + 0.06 \cdot F \tag{10}$$

where

$$F = \eta \left(1 - \left(((x - x_c)/x_c)^2 + ((y - y_c)/y_c)^2 \right) \Big/ 2 \right) + (1 - \eta) \cdot (0.4 \cdot \exp(-r_i) + 0.35 \cdot \exp(-r_i) + 0.25 \cdot \exp(r_i)) \tag{11}$$

wherein Eq (11), r_i can further be expressed as,

Table 1
Parameters of the selected transitions at around 7185.60 cm^{-1} and 7444.36 cm^{-1}.

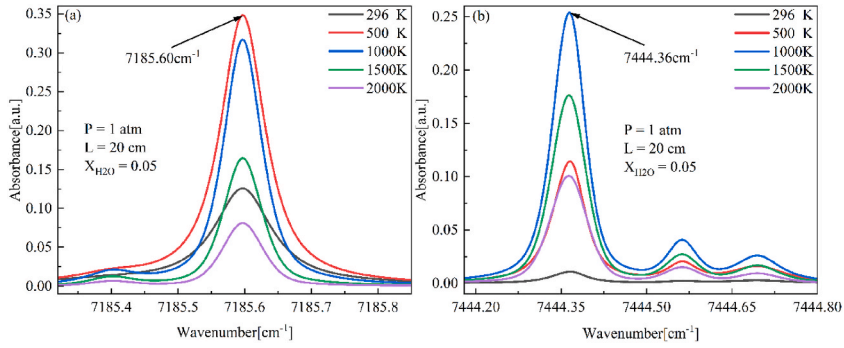| line index	Wavenumber (cm^{-1})	$S(T_0)$ (cm^{-2}atm^{-1})	ξ_{self} (cm^{-1}atm^{-1})	ξ_{air} (cm^{-1}atm^{-1})	E'' (cm^{-1})	n_{air}
1	7185.596	0.00490	0.371	0.0342	1045.0583	0.63
	7185.597	0.0147	0.195	0.0413	1045.058	0.65
2	7444.351	0.000541	0.366	0.0199	1774.750	0.44
	7444.368	0.000154	0.250	0.0188	1806.670	0.41
	7444.371	0.000462	0.194	0.0153	1806.669	0.41

Fig. 3. Simulated H_2O absorbance spectra for transitions near 7185.60 cm^{-1} (a) and 7444.36 cm^{-1} (b) at different temperatures and a particular concentration. The total pressure and path length were set at 1 atm and 20 cm, respectively.
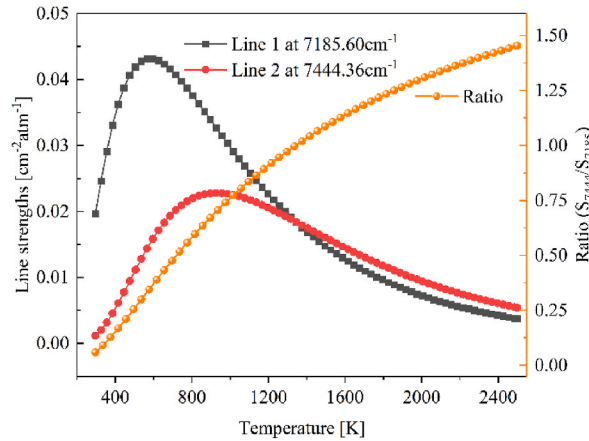

Fig. 4. Line strengths and ratio of the line strengths of these two H_2O absorption transitions at 7185.60 cm^{-1} and 7444.36 cm^{-1}.

$$r_i = ((x - x_i)/\sigma)^2 + ((y - y_i)/\sigma)^2 \quad i = 1, 2, 3 \tag{12}$$

where x_c and y_c denote the center coordinate $(x_c, y_c) = (10,10)$, η is the weighting factor $\eta = 0.2$, σ is the Gaussian distribution parameter $\sigma = 4$. For the non-axisymmetric temperature model, the peaks are located at coordinates $(x_1, y_1) = (6, 14)$, $(x_2, y_2) = (14, 14)$ and $(x_3, y_3) = (9, 6)$, respectively.

The optical arrangement is shown in Fig. 5. The optimal optical path is arranged according to the on-site measurement of the afterburner, which can meet the multi-angle arrangement of 100 laser beams.

To quantify reconstruction fidelity, the reconstruction error between the phantom and reconstruction is defined as
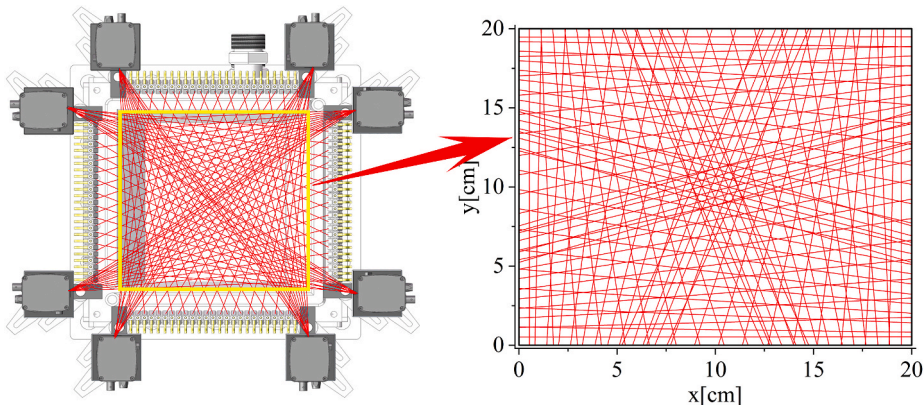

Fig. 5. Optical arrangement of the designed sensor.

$$e = \left\| \overrightarrow{x}^{exact} - \overrightarrow{x}^{rec} \right\|_2 / \left\| \overrightarrow{x}^{exact} \right\|_2 \qquad (13)$$

where $\overrightarrow{x}^{exact}$ and $\overrightarrow{x}^{rec}$ represent the variables of phantom and the reconstruction, respectively, and $\|\cdot\|_2$ denotes the 2-norm of a vector.

In a tomographic reconstruction, the region of interest (ROI) is usually divided into a number of square grids, in each of which the values of the reconstruction parameters are assumed to be constant. Therefore, the size of the grid determines the spatial resolution of the measurement. The smaller the grid size is, the higher the spatial resolution will be. But as the grid size becomes smaller and the grid number increases, the risk of reconstruction ill-posedness rises, resulting in poorer reconstruction quality [30]. To balance these two targets, in the simulation, the optimized resolution was sought over the grid number range of 80 × 80 to 160 × 160.

Generally, in engine afterburner applications, the acquired signals are affected by noises such as mechanical vibration and thermal radiation. To assess the system performance in a noisy environment, different levels of random noise varied from 1% to 8% of the absorption data were applied. The variation of reconstruction errors with grid number under different noise levels are shown in Fig. 6.

The performance of the test sensor was analyzed by comparing the reconstruction errors for five different reconstruction grid numbers at eight different noise levels. The results are shown in Fig. 6, where the vertical coordinate represents the reconstruction errors for the temperature and water vapor concentration. It can be seen from the diagram that the reconstruction quality for either temperature or concentration decreases as the noise level increases. The temperature and concentration reconstruction errors also rise gradually with increase of grid number. It is evident that the reconstruction errors for both temperature and concentration surge at the grid 140 × 140. In order to balance the two factors of reconstruction resolution and quality, the 120 × 120 grid resolution was finally selected as the main research object, i.e., 100 emitted laser paths were realized in a limited space of 200mm×200 mm with a minimum spatial resolution of 1.67mm×1.67 mm.

It can be seen that the reconstructed images of the temperature and water vapor molar concentration distributions depicted in Fig. 7 (b)and(e) resemble, the phantoms set in (a)and(d), and even with a severe noise imposed, the reconstructed images in Fig. 7 (c) and (f) still retain the main features of original phantoms, demonstrating the excellent stability and robustness of the system.

3.3. Hardware design

The proposed LAS tomography sensor of the afterburner was prototyped for field tests, which is shown in Fig. 8. The sensor consists of six units, namely the afterburner test section, thermocouple measurement unit, laser beam switcher, signal generator and receiver, signal acquisition, and a host PC.

The afterburner is made of special stainless-steel plates with a cooling water jacket outer wall. The outlet size of the afterburner is 200 mm×200 mm. The burner inlet is supplied with high-pressure air, and the oil supply nozzles are installed in the burner duct. The oil-gas mixture is ignited by electric sparks. Both air and oil are precisely controlled to maintain constant flammability throughout the experiment.

The temperature distribution references over the entire afterburner outlet are obtained using 81 K-type thermocouples, which are arranged as a 9 × 9 matrix over the cross-section, where the LAS measurement sensor is installed on the same plane.

Two distributed feedback (DFB) diodes with laser beams operating near 7185.60 cm-1 (NTT, NLK1E5GAAA) and 7444.36 cm-1 (NTT, NLK1B5EAAA) are adopted to probe the H2O transitions. To achieve wavelength modulation, the injection current was driven by the Data Acquisition device (DAQ, NI Corporation, PCI6115) which provided a 1 kHz sinusoidal scan signal superimposed with a 100 kHz sinusoidal modulation signal. The two lasers were operated in time division multiplexing (TDM) mode. The signal function is given by the PC. The two laser beams are combined and then split by a 2 × 2 single-mode fiber-coupler. One output of the fiber-coupler is guided through an etalon with a free spectral range (FSR) of 0.01 cm^{-1} for wavelength monitoring and the other output passes into the optical switch(custom-made).

The optical switch can realize laser beam 1 channel input and 100 channels output. The optical switch toggles the input laser beam to the different output laser beams through a switcher with a time interval of 10 ms. The switching loss for each channel of the optical switch is only 0.2 dB. There are also other laser power losses in the sensor, such as long-distance fiber attenuation loss and insertion loss
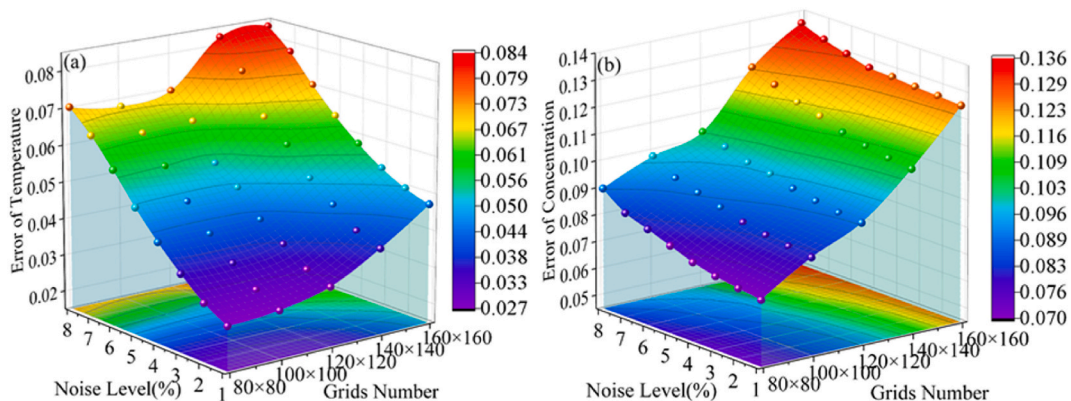

Fig. 6. 3D plot of reconstruction errors for temperature (a) and water vapor molar concentration (b) for different grids.
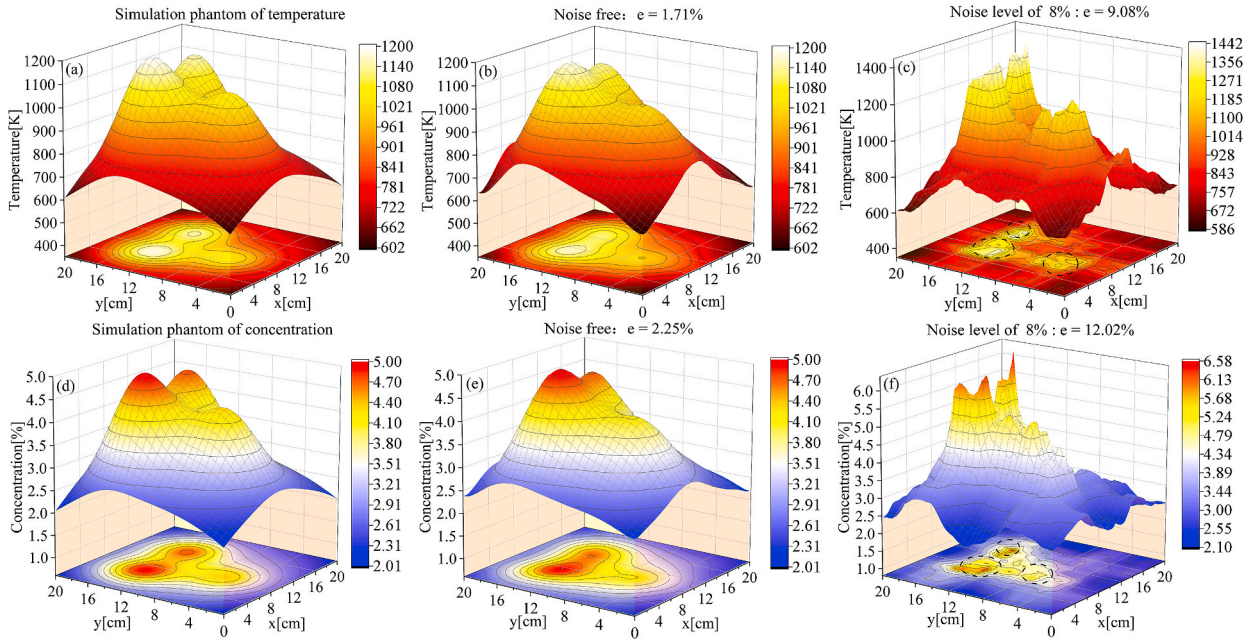
Fig. 7. Reconstruction domain with 120×120 discretized grids. (a)and(d) Simulation set up for temperature and water vapor concentration phantoms. (b) and (e) Noise free reconstructed distributions of the phantoms. (c)and(f) Reconstructed phantoms with added uniform noise at level of 8%.
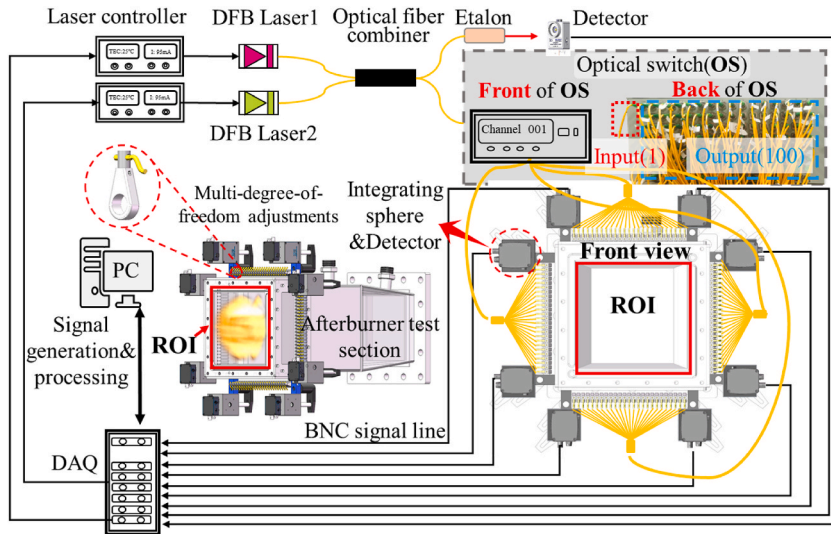

Fig. 8. The tomography sensor based on LAS on the afterburner.

between fibers, etc. The laser power of the sensor is measured by an optical power meter (Thorlabs, PM101-S120C), as shown in Table 2. The sensor has 100 laser beams installed. Each of the 25 laser beams is collected and mounted on one side of the burner. A new miniaturized laser emission module shown in Fig. 8 was purposely designed for achieving multi-degree of freedom adjustment and reducing the attenuation of laser power. It takes 1 s to complete the reconstruction of an image.

The DAQ card is for synchronizing receiving and transmitting signals. The digitization rates for sampling of the absorption signal are 10 Mega samples per second. Compared with other currently used sensors, this proposed sensor can not only reduce the cost for the signal reception and acquisition considerably but also improve the spatial resolution. This is certainly a significant improvement considering the small number of detectors utilized only in the sensor.

Table 2
The output power of each laser beam tested by the optical power meter.

| Input power [mW]	Sequence number	Output power [mW]	Sequence number	Output power [mW]	Sequence number	Output power [mW]	Sequence number	Output power [mW]
4.52	1	2.78	26	2.64	51	2.37	76	2.37
	2	2.95	27	2.35	52	2.64	77	2.54
	3	2.34	28	2.34	53	2.19	78	2.94
	4	2.48	29	3.01	54	2.64	79	2.61
	5	2.39	30	2.64	55	2.48	80	2.32
	6	2.49	31	2.84	56	2.38	81	2.47
	7	2.16	32	2.85	57	2.15	82	2.52
	8	2.49	33	2.65	58	2.67	83	2.34
	9	2.79	34	2.34	59	2.94	84	2.27
	10	2.64	35	2.79	60	2.58	85	2.14
	11	2.54	36	2.65	61	2.34	86	2.94
	12	2.19	37	2.31	62	2.74	87	2.82
	13	2.65	38	2.49	63	2.64	88	2.62
	14	2.94	39	2.67	64	2.51	89	2.38
	15	2.31	40	2.16	65	2.31	90	2.25
	16	2.57	41	2.65	66	2.54	91	2.64
	17	2.65	42	2.94	67	2.38	92	2.43
	18	2.49	43	2.79	68	2.79	93	2.57
	19	2.13	44	2.37	69	2.83	94	2.34
	20	2.29	45	2.61	70	2.48	95	2.37
	21	2.27	46	2.54	71	2.61	96	2.64
	22	2.49	47	2.15	72	2.51	97	2.81
	23	2.62	48	2.34	73	2.38	98	2.38
	24	2.32	49	2.67	74	2.39	99	2.61
	25	2.64	50	2.49	75	2.37	100	2.67

4. Experiments results and discussion

4.1. Analysis of received laser intensity signal through experiments

There are several technical challenges to overcome before an optical sensor can be applied in practical measurement in real afterburners. Firstly, the optical access to the afterburner must be temperature resistant, and chemically inert. Therefore, quartz glass viewing windows and special stainless-steel components were chosen to protect the optical sensor in the proposed sensor. Secondly, during the afterburner operation, access is usually prohibited for safety reasons and no alignment of the sensor can be performed, hence the optical sensor was pre-adjusted prior to its installation. In addition, there were many unavoidable factors that reduce the laser transmission in the experiments, including dust scattering in the open path structure, contamination of the glass window sheet by black unburned carbon in the flame, optical misalignment, mechanical vibrations, turbulent disturbances, etc.

In order to verify the noise immunity of the proposed sensor, experiments were carried out at the exit of the afterburner. Two different receiving optical paths were used for the analysis, which are shown in Fig. 9(a). In many cases where a sensor is used with the conventional method, only one focusing lens is placed in front of the detector (C-Detector) for receiving laser beams. In such a sensor, the received signal is often susceptible to violent mechanical vibrations and turbulent flame combustion inside the engine. The sensor proposed in this paper provides a solution to this problem by replacing the focusing lens with an integrating sphere, which is combined with a detector (IS-Detector) to form the laser beam receiver. The experiment results confirmed that the received signal became much more stable through the above alteration.

Shown in Fig. 9(b) are the signals obtained via the experiments, which apparently reveal that the measured light intensity by the C-
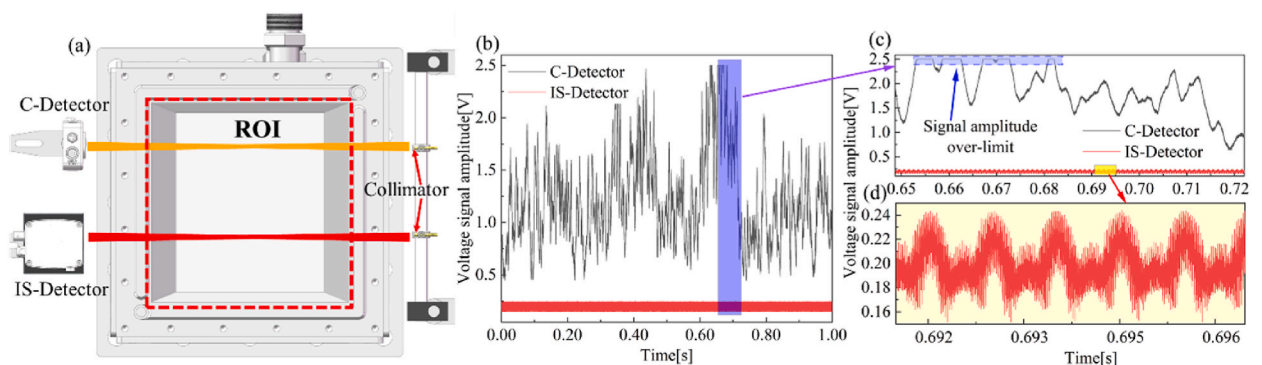
Fig. 9. Two different receiving optical paths, (a) The structures optical path (b) Received voltage signal (c) Local zoom of the both voltage signal (d) Local zoom of the IS-detector signal.

Detector severely jittered and deviated from the target surface of the detector due to the mechanical vibration of the device and gas turbulence, causing distortion of the sampled signal. In addition, as shown in Fig. 9(c), the detection limit of the signal is exceeded due to the thermal radiation of the flame. In contrast to the C-detector sensor, it can be seen in Fig. 9(d) that the signal received by the IS-Detector was not affected by the harsh combustion environment at all. This confirms that the IS-Detector method has a much-improved robustness due to the novel design.

4.2. Reconstruction results based on experiments and discussion

The experiments for field temperature and concentration reconstruction were conducted at the exit of the afterburner under, two different operating conditions: the main engine combustion and the afterburner operation. The main engine combustion is a normal engine operating condition, whilst the afterburner operation is in a state where an engine secondary ignition occurs, which takes place mainly in the aircraft pursuit and escape situation. Similar to a real engine, the afterburner rig consists of the systems of air inlet, oil supply, ignition, and water cooling. During the experiments, the air inlet system provided the compressed air with its parameters (pressure, inlet volume, etc.) precisely controlled. The oil supply system fed the required amount of oil into the afterburner to achieve the above two given combustion states. The oil and gas were merged in the combustion chamber, their mixture was ignited. When the combustion state was stable, the proposed sensor started to perform the measurement.

The 9×9 thermocouple measurement temperature matrix was arranged and 120×120 grids were used for the LAS reconstruction. The thermocouple array was installed in the same plane as the laser beam photodetectors installation to facilitate the temperature comparison with the LAS reconstruction results so that evaluation of the measurement accuracy could be conducted. To evaluate the accuracy of the LAS reconstruction, temperature values from the LAS reconstructed temperature at the same location as the thermocouple measurement were found for comparison.

Fig. 10 shows the two-dimensional reconstruction of the temperature distribution in the main combustion state. From Fig. 10 (a) and (b), it can be seen that the LAS reconstructed temperature distribution is consistent with the measurement results obtained from the thermocouple array. From Fig. 10(c), The maximum error was about 4.32%.

Fig. 11 display the two-dimensional reconstruction of the temperature distribution in the afterburner operation. Unlike in the main combustion state, the reconstruction maps in this display a high temperature zone on the left side of the combustion exit by the LAS. The high temperature zone formed in this state was due to that the oil supply system accelerated combustion near the left side of the pipe in the experiment, causing unbalanced heating up on this side. From Fig. 11 (c), it can be seen that the higher relative error occurred mainly near some parts around the edge area, and the maximum error was about 5.38%. This result is consistent with the reconstruction results of the literature [16,30,31]. To improve the reconstruction quality, more suitable smoothing regularization parameters can be found. It can also be introduced with advanced reconstruction algorithms [32–36].

The concentration reconstruction via the experiments is shown in Fig. 12. As there is no other method for obtaining the accurate concentration distribution of water vapor, the comparison performed for the concentration could not be performed directly. However, in hydrocarbon flames, the water vapor concentration is usually well-correlated with the temperature. Therefore, the water vapor concentration distribution in each phantom is similar to the temperature distribution. The water vapor concentration distribution in this result is in agreement with the trend of the temperature distribution, which, to a certain extent, demonstrates the effectiveness of the concentration reconstruction using the proposed method.

From the experiment reconstruction results under the two different states of the acceleration combustion, it can be concluded that the proposed sensor is superior over other LAS measurement sensors regarding both the measurement stability and accuracy. It can be envisaged that this sensor can be applied under complex combustion conditions in the near future.

5. Conclusions

This paper presents a tomographic measurement sensor based on the LAS technology for aero-engine afterburner flames reconstruction. In the concerned sensor, a novel receiver has been designed which adopts an integrating sphere connected to a detector. With this design the requirement for laser collimation and alignment are much less stringent, even in extremely harsh environments, and the interference stripes in the received laser signals are eliminated so that the stability of the laser signals is improved. In addition, the proposed LAS sensor includes a set of purpose-designed miniaturized laser transmitter modules, which have the capability for adjustment with multi-degree of freedom, thus the attenuation of laser power is mitigated. With merely 8 sets of receivers, the entire optical path can be captured. Operating at such a small number of receivers, the equipment cost is significantly reduced whilst the measurement spatial resolution is significantly improved. In effect, 100 emitted laser paths have been achieved in a limited space of 200 mm $\times$ 200 mm with a spatial resolution of 1.67 mm $\times$ 1.67 mm. The performance of the system was evaluated by comparing the reconstruction errors at five different reconstruction grids (spatial resolutions) and eight different noise levels through simulation analysis. The reconstruction results show that the quality of both temperature and concentration reconstructions deteriorated with noise levels increase, however the reconstructions retain the main features of the original temperature and water vapor concentration even at the noise level as high as 8%.

The proposed system was also validated through field experiments. Two signal reception methods were compared through the experiments in an afterburner. The C-Detector method used in conventional systems was proved to encounter serious signal interference during the experiments. In contrast, the IS-Detector demonstrated its advantages of receiving stable signal, showing strong immunity to any noises of the harsh combustion environments. The performance of the system was verified through the field experiments under two different states in the afterburner, and it was shown from the reconstruction results that the error at the main combustion state was about 4.32% and the error for the afterburner operation state was within 5.38% for the temperature
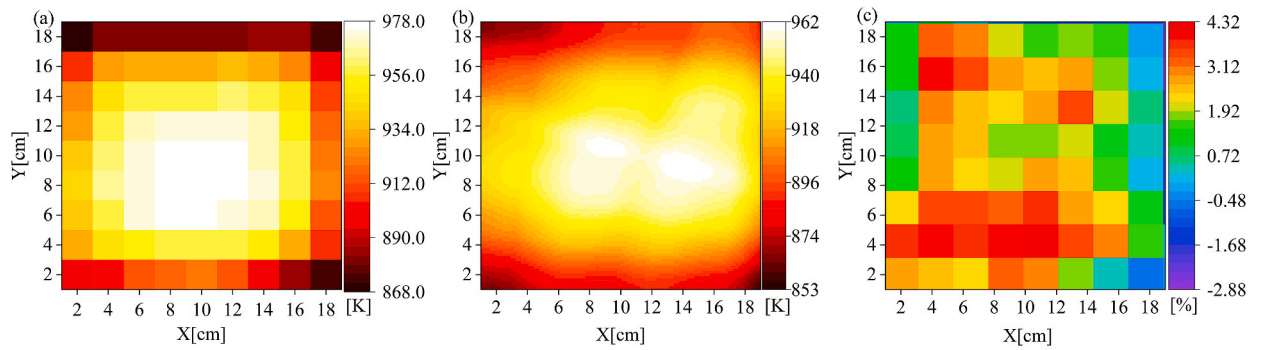
Fig. 10. Two-dimensional reconstruction of temperature distribution in the main combustion, (a) the reconstructed result of thermocouple array; (b) the reconstructed result of TDLAS; (c) the reconstructed relative error.
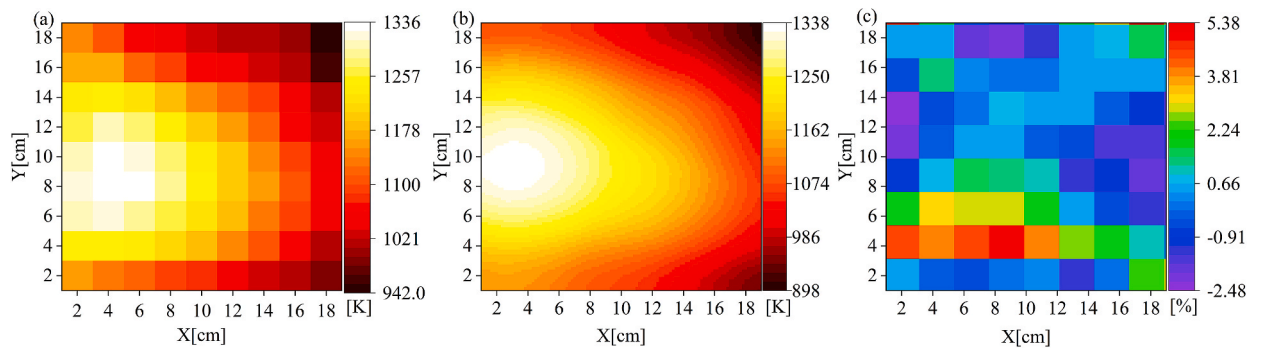

Fig. 11. Two-dimensional reconstruction of temperature distribution in afterburner operation, (a) the reconstructed result of thermocouple array; (b) the reconstructed result from LAS; (c) reconstructed relative error.
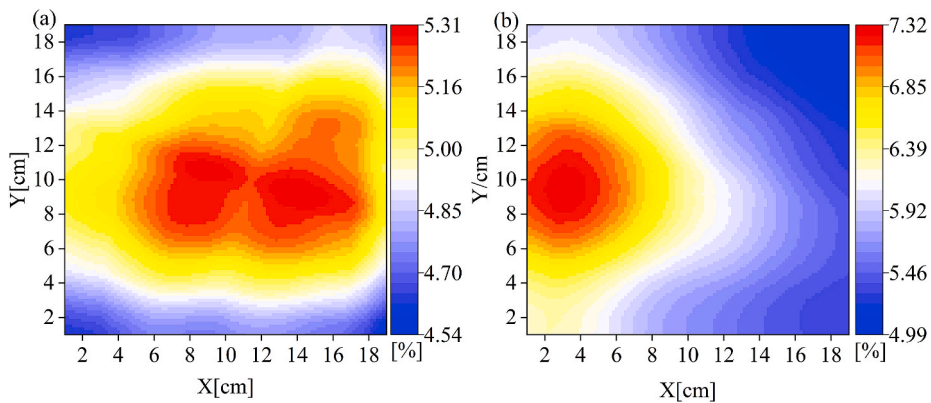

Fig. 12. Two-dimensional reconstruction of concentration distribution (a) the main combustion; (b) the afterburner operation.

reconstructions with the references to the thermocouple measurement data. These results demonstrate the significant improvement in terms of accuracy and robustness, it can be expected that the proposed technology in this paper to find its wide applications in industries.

Author statement

Rong Zhao: Ideas, Methodology, Software. Bin Zhou: Formal analysis, Resources, Supervision. Jianyong Zhang: Data Curation, Software. Ruixue Cheng: Visualization, Investigation. Qi Liu: Discussion and guidance on experimental details. Minglu Dai: Data Curation, Software. Bubin Wang: Assist with experiments. Yihong Wang: Writing- Reviewing and Editing.

Declaration of competing interest

The authors declare that they have no known competing financial interests or personal relationships that could have appeared to influence the work reported in this paper.

Data availability

Data will be made available on request.

References

[1] M. Dai, B. Zhou, J. Zhang, B. Zuo, Y. Wang, Experimental and simulation investigation of 3-D soot temperature and volume fraction fields of afterburner flame, Case Stud. Therm. Eng. 33 (2022), 101932, https://doi.org/10.1016/j.csite.2022.101932.

[2] Mixing and transient combustion processes of scramjet combustor with transverse injector and hypermixer, Case Stud. Therm. Eng. 26 (2021), 101104, https://doi.org/10.1016/j.csite.2021.101104.

[3] M. Stöhr, I. Boxx, C.D. Carter, W. Meier, Experimental study of vortex-flame interaction in a gas turbine model combustor, Combust. Flame 159 (2012) 2636–2649, https://doi.org/10.1016/j.combustflame.2012.03.020.

[4] L. Ma, X.S. Li, S.T. Sanders, A.W. Caswell, S. Roy, D.H. Plemmons, J.R. Gord, 50-kHz-rate 2D imaging of temperature and H2O concentration at the exhaust plane of a J85 engine using hyperspectral tomography, Opt Express 21 (2013) 1152–1162, https://doi.org/10.1364/oe.21.001152.

[5] Q. Liu, B. Zhou, J. Zhang, R. Cheng, M. Dai, X. Zhao, Y. Wang, A novel time-of-flight estimation method of acoustic signals for temperature and velocity measurement of gas medium, Exp. Therm. Fluid Sci. 140 (2022), 110759, https://doi.org/10.1016/j.expthermflusci.2022.110759.

[6] Q. Liu, B. Zhou, J. Zhang, R. Cheng, X. Zhao, R. Zhao, M. Dai, B. Wang, Y. Wang, A time-of-flight estimation method for acoustic ranging and thermometry based on digital lock-in filtering, Sensors 22 (2022) 5519, https://doi.org/10.3390/s22155519.

[7] Q. Liu, B. Zhou, J. Zhang, R. Cheng, Development of flue gas audio-range velocimeter using quadratic-convex frequency sweeping, IEEE Sensor. J. 21 (2021) 9777–9787, https://doi.org/10.1109/JSEN.2021.3055343.

[8] Q. Liu, B. Zhou, R. Cheng, J. Zhang, Y. Wang, High temporal resolution pyrometry and velocimetry based on acoustic frequency division multiplexing, IEEE Trans. Instrum. Meas. 71 (2022) 1–11, https://doi.org/10.1109/TIM.2022.3141169.

[9] A. Bohlin, E. Nordström, H. Carlsson, X. Bai, P.-E. Bengtsson, Pure rotational CARS measurements of temperature and relative O2-concentration in a low swirl turbulent premixed flame, Proc. Combust. Inst. 34 (2013) 3629–3636, https://doi.org/10.1016/j.proci.2012.05.016.

[10] Y. Wang, B. Zhou, C. Liu, Calibration-free wavelength modulation spectroscopy based on even-order harmonics, Opt Express 29 (2021) 26618–26633, https://doi.org/10.1364/OE.432361.

[11] Y. Wang, B. Zhou, C. Liu, Sensitivity and accuracy enhanced wavelength modulation spectroscopy based on PSD analysis, IEEE Photon. Technol. Lett. 33 (2021) 1487–1490, https://doi.org/10.1109/LPT.2021.3128448.

[12] H. McCann, P. Wright, K. Daun, S.J. Grauer, C. Liu, S. Wagner, Chemical species tomography, in: Ind. Tomogr., Elsevier, 2022, pp. 155–205. https://linkinghub.elsevier.com/retrieve/pii/B9780128230152000042. (Accessed 18 May 2022).

[13] R. Zhang, J. Si, G. Enemali, Y. Bao, C. Liu, Spatially driven chemical species tomography with size-adaptive hybrid meshing scheme, IEEE Sensor. J. 22 (2022) 12728–12737.

[14] C. Liu, L. Xu, F. Li, Z. Cao, S.A. Tsekenis, H. McCann, Resolution-doubled one-dimensional wavelength modulation spectroscopy tomography for flame flatness validation of a flat-flame burner, Appl. Phys. B 120 (2015) 407–416, https://doi.org/10.1007/s00340-015-6150-9.

[15] Liu Chang, Cao Zhang, Yuzhen Lin, Lijun Xu, Hugh McCann, online cross-sectional monitoring of a swirling flame using TDLAS tomography, IEEE Trans. Instrum. Meas. 67 (2018) 1338–1348, https://doi.org/10.1109/TIM.2018.2799098.

[16] J. Song, Y. Hong, M. Xin, G. Wang, Z. Liu, Tomography system for measurement of gas properties in combustion flow field, Chin. J. Aeronaut. 30 (2017) 1697–1707, https://doi.org/10.1016/j.cja.2017.08.004.

[17] Y. Zhai, F. Wang, Y. Chi, K. Cen, Optical absorption tomography for temperature and H₂O concentration imaging by a compact photoelectric detecting system combined with twice adaptive algebraic algorithm, Opt. Eng. 61 (2022), 034103, https://doi.org/10.1117/1.OE.61.3.034103.

[18] H. Xia, R. Kan, Z. Xu, Y. He, J. Liu, B. Chen, C. Yang, L. Yao, M. Wei, G. Zhang, Two-step tomographic reconstructions of temperature and species concentration in a flame based on laser absorption measurements with a rotation platform, Opt Laser. Eng. 90 (2017) 10–18, https://doi.org/10.1016/j.optlaseng.2016.09.005.

[19] Z. Wang, W. Zhou, J. Yan, T. Kamimoto, K. Tsujimoto, Y. Li, Y. Deguchi, N.A. Sani, S.H. Samsuri, M.F. Zulkifli, Application of 2D temperature measurement to a coal-fired furnace using CT-TDLAS, Meas. Sci. Technol. 31 (2020), 035203, https://doi.org/10.1088/1361-6501/ab4f05.

[20] C. Liu, Z. Cao, F. Li, Y. Lin, L. Xu, Flame monitoring of a model swirl injector using 1D tunable diode laser absorption spectroscopy tomography, Meas. Sci. Technol. 28 (2017), 054002, https://doi.org/10.1088/1361-6501/aa5aee.

[21] L. Xu, C. Liu, W. Jing, Z. Cao, X. Xue, Y. Lin, Tunable diode laser absorption spectroscopy-based tomography system for on-line monitoring of two-dimensional distributions of temperature and H ₂ O mole fraction, Rev. Sci. Instrum. 87 (2016), 013101, https://doi.org/10.1063/1.4939052.

[22] Wenyang Jing, Cao Zhang, Hongyu Zhang, Qianwei Qu, Lijun Xu, A reconfigurable parallel data acquisition system for tunable diode laser absorption spectroscopy tomography, IEEE Sensor. J. 17 (2017) 8215–8223, https://doi.org/10.1109/JSEN.2017.2652497.

[23] P. Wright, N. Terzija, J.L. Davidson, S. Garcia-Castillo, C. Garcia-Stewart, S. Pegrum, S. Colbourne, P. Turner, S.D. Crossley, T. Litt, High-speed chemical species tomography in a multi-cylinder automotive engine, Chem. Eng. J. 158 (2010) 2–10.

[24] S.J. Grauer, K.M. Rice, J.M. Donbar, N.J. Bisek, J.J. France, B.A. Ochs, A.M. Steinberg, Optimization of tunable diode laser arrays for inlet mass capture measurement, AIAA J. (2022) 1–14, https://doi.org/10.2514/1.J061774.

[25] W.S. Zhao, L.J. Xu, A. Huang, X. Gao, X.Z. Luo, H.Y. Zhang, H.T. Chang, Z. Cao, A WMS based TDLAS tomographic system for distribution retrievals of both gas concentration and temperature in dynamic flames, Ieee Sens. J. 20 (2020) 4179–4188, https://doi.org/10.1109/jsen.2019.2962736.

[26] C. Shui, Y. Wang, W. Cai, B. Zhou, Linear multispectral absorption tomography based on regularized iterative methods, Opt Express 29 (2021) 20889–20912, https://doi.org/10.1364/OE.421817.

[27] J.L. Song, Y.J. Hong, G.Y. Wang, H. Pan, Algebraic tomographic reconstruction of two-dimensional gas temperature based on tunable diode laser absorption spectroscopy, Appl. Phys. B Laser Opt. 112 (2013) 529–537, https://doi.org/10.1007/s00340-013-5435-0.

[28] N. Li, C. Weng, Modified adaptive algebraic tomographic reconstruction of gas distribution from incomplete projection by a two-wavelength absorption scheme, Chin. Opt Lett. 9 (2011), https://doi.org/10.3788/col201109.061201, 061201–061205.

[29] I.E. Gordon, L.S. Rothman, C. Hill, R.V. Kochanov, Y. Tan, P.F. Bernath, M. Birk, V. Boudon, A. Campargue, K.V. Chance, B.J. Drouin, J.-M. Flaud, R.R. Gamache, J.T. Hodges, D. Jacquemart, V.I. Perevalov, A. Perrin, K.P. Shine, M.-A.H. Smith, J. Tennyson, G.C. Toon, H. Tran, V.G. Tyuterev, A. Barbe, A.G. Császár, V.M. Devi, T. Furtenbacher, J.J. Harrison, J.-M. Hartmann, A. Jolly, T.J. Johnson, T. Karman, I. Kleiner, A.A. Kyuberis, J. Loos, O.M. Lyulin, S.T. Massie, S.N. Mikhailenko, N. Moazzen-Ahmadi, H.S.P. Müller, O.V. Naumenko, A.V. Nikitin, O.L. Polyansky, M. Rey, M. Rotger, S.W. Sharpe, K. Sung, E. Starikova, S.A. Tashkun, J.V. Auwera, G. Wagner, J. Wilzewski, P. Wcisło, S. Yu, E.J. Zak, The HITRAN2016 molecular spectroscopic database, J. Quant. Spectrosc. Radiat. Transf. 203 (2017) 3–69, https://doi.org/10.1016/j.jqsrt.2017.06.038.

[30] T. Yu, W. Cai, Benchmark evaluation of inversion algorithms for tomographic absorption spectroscopy, Appl. Opt. 56 (2017) 2183.

[31] A. Huang, Z. Cao, W. Zhao, H. Zhang, L. Xu, Frequency-division multiplexing and main peak scanning WMS method for TDLAS tomography in flame monitoring, IEEE Trans. Instrum. Meas. 69 (2020) 9087–9096, https://doi.org/10.1109/tim.2020.2998935.

[32] Y. Bao, R. Zhang, G. Enemali, Z. Cao, B. Zhou, H. McCann, C. Liu, Relative entropy regularized TDLAS tomography for robust temperature imaging, IEEE Trans. Instrum. Meas. 70 (2021) 1–9, https://doi.org/10.1109/TIM.2020.3037950.

[33] A. Deng, J. Huang, H. Liu, W. Cai, Deep learning algorithms for temperature field reconstruction of nonlinear tomographic absorption spectroscopy - ScienceDirect, 10–12, Meas. Sens. s (2020) 10–12.

[34] J. Huang, J. Zhao, W. Cai, Compressing convolutional neural networks using POD for the reconstruction of nonlinear tomographic absorption spectroscopy, Comput. Phys. Commun. 241 (2019) 33–39, https://doi.org/10.1016/j.cpc.2019.03.020.

[35] Xin Gao, Cao Zhang, Hongyao Li, Fanghao Lu, Ang Huang, Lijun Xu, Sparse Zernike fitting for dynamic LAS tomographic images of temperature and water vapor concentration, IEEE Trans. Instrum. Meas. (2022), https://doi.org/10.1109/tim.2022.3165802, 1–1.

[36] C. Shui, J. Huang, H. Liu, W. Cai, S.T. Sanders, Tomographic absorption spectroscopy based on dictionary learning, Opt Express 29 (2021), https://doi.org/10.1364/oe.440709.